Femtosecond Stimulated Raman Spectroscopy of the Cyclobutane Thymine Dimer Repair Mechanism: A Computational Study

Hideo Ando,[†] Benjamin P. Fingerhut,[‡] Konstantin E. Dorfman,[†] Jason D. Biggs,[†] and Shaul Mukamel*,[†]

[†]Department of Chemistry, 1102 Natural Sciences II, University of California, Irvine, California 92697-2025, United States
[‡]Max-Born-Institut für Nichtlineare Optik und Kurzzeitspektroskopie, Max-Born-Strasse 2A, 12489 Berlin, Germany

S *Supporting Information*

ABSTRACT: Cyclobutane thymine dimer, one of the major lesions in DNA formed by exposure to UV sunlight, is repaired in a photoreactivation process, which is essential to maintain life. The molecular mechanism of the central step, i.e., intradimer C—C bond splitting, still remains an open question. In a simulation study, we demonstrate how the time evolution of characteristic marker bands (C=O and C=C/C—C stretch vibrations) of cyclobutane thymine dimer and thymine dinucleotide radical anion, thymidylyl($3' \rightarrow 5'$)-thymidine, can be directly probed with femtosecond stimulated Raman spectroscopy (FSRS). We construct a DFT(M05-2X) potential energy surface with two minor barriers for the intradimer C_5—C_5' splitting and a main barrier for the C_6—C_6' splitting, and identify the appearance of two C_5=C_6 stretch vibrations due to the C_6—C_6' splitting as a spectroscopic signature of the underlying bond splitting mechanism. The sequential mechanism shows only absorptive features in the simulated FSRS signals, whereas the fast concerted mechanism shows characteristic dispersive line shapes.
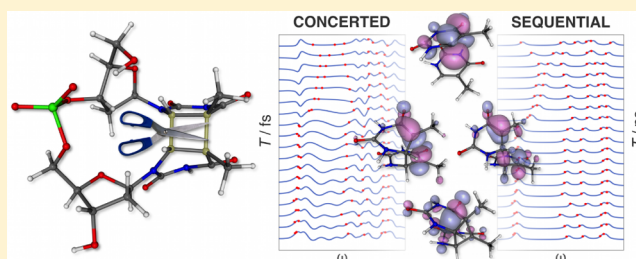
1. INTRODUCTION

The photoinduced excited-state dynamics of DNA is of great importance in biology, medicine, and life science. The exposure of living organisms to UV sunlight causes harmful lesions to DNA. One of the major lesions is cyclobutane pyrimidine dimer (CPD),[1−5] which is formed through [2+2] photo-cycloaddition and may eventually lead to skin cancer. Living organisms often use specific flavoproteins, CPD-photolyase (PL), to repair the lesions in DNA sequences using a blue light activated enzymatic cycle (see Scheme 1).[6,7] Macroscopically, this photoreactivation process satisfies Michaelis−Menten kinetics, where CPD-containing DNA is bound to the redox cofactor flavin-adenine dinucleotide (FADH⁻) in CPD-PL and light acts as splitting agent.[8−10] Recent ultrafast time-resolved transient absorption experiments[6,7] and simulations[11−14] revealed that the microscopic photoreactivation mechanism involves three steps as summarized in Scheme 1: electron transfer from excited FADH⁻ to CPD, splitting of intradimer C—C bonds in CPD, and electron return to restore catalytically active FADH⁻, whose rates are well optimized to ensure a high repair quantum yield (about 0.5−1.0).[2,6,7]

The entire photoreactivation process is completed within one nanosecond.[15] For the second and central step of the intradimer C—C bond cleavage, a number of transient absorption studies have been carried out to clarify the kinetics. In the overall splitting process of the two C—C bonds, however, there is controversy due to the lack of unique molecular probes. Barrierless formation of one C_5=C_6 double bond upon electron transfer was observed within 60 ps by

MacFarlane and Stanley[16] and later associated with overall C—C splitting by Masson et al.[14] Thiagarajan et al.,[7] Kao et al.,[15] and Langenbacher et al.[17] proposed slower splitting rates (i.e., 260 ps, <560 ps, and no splitting below 200 K), and an overall barrier was estimated to be 10.7 ± 2.3 kcal/mol.[17] Besides, transient absorption results by Liu et al. suggested that CPD splitting occurs in a sequential mechanism,[6] where the two bonds are broken in a stepwise manner: 10 ps splitting of the C_5—C_5' bond, followed by 90 ps splitting of the C_6—C_6' bond (see Scheme 1). In contrast, theoretical investigations of CPD embedded in the active site of CPD-PL[14] and in DNA duplex[18] suggest ultrafast CPD splitting in an (asynchronous) concerted mechanism, whereby the C_5—C_5' bond splits upon electron uptake within 10−100 fs and the C_6—C_6' bond splits within a few picoseconds. Interpretation of visible-light probe studies is difficult because relevant radical reaction intermediates as well as other radicals arising from photoreactivation processes absorb in this region.[2] On the other hand, UV probes[16] monitor the appearance of repaired thymine, but provide only limited sensitivity for transient radical intermediates. Details of the splitting mechanism remain an open question and a direct spectroscopic probe of the molecular rearrangements upon the CPD splitting pathway is yet to be reported.

Time- and frequency-resolved vibrational spectroscopy with infrared or Raman probes can closely follow specific atomic motions. Unique vibrational bands serve as fingerprints of the

Scheme 1. Proposed Photoreactivation Mechanism of the CPD Lesion by CPD-PL[a]
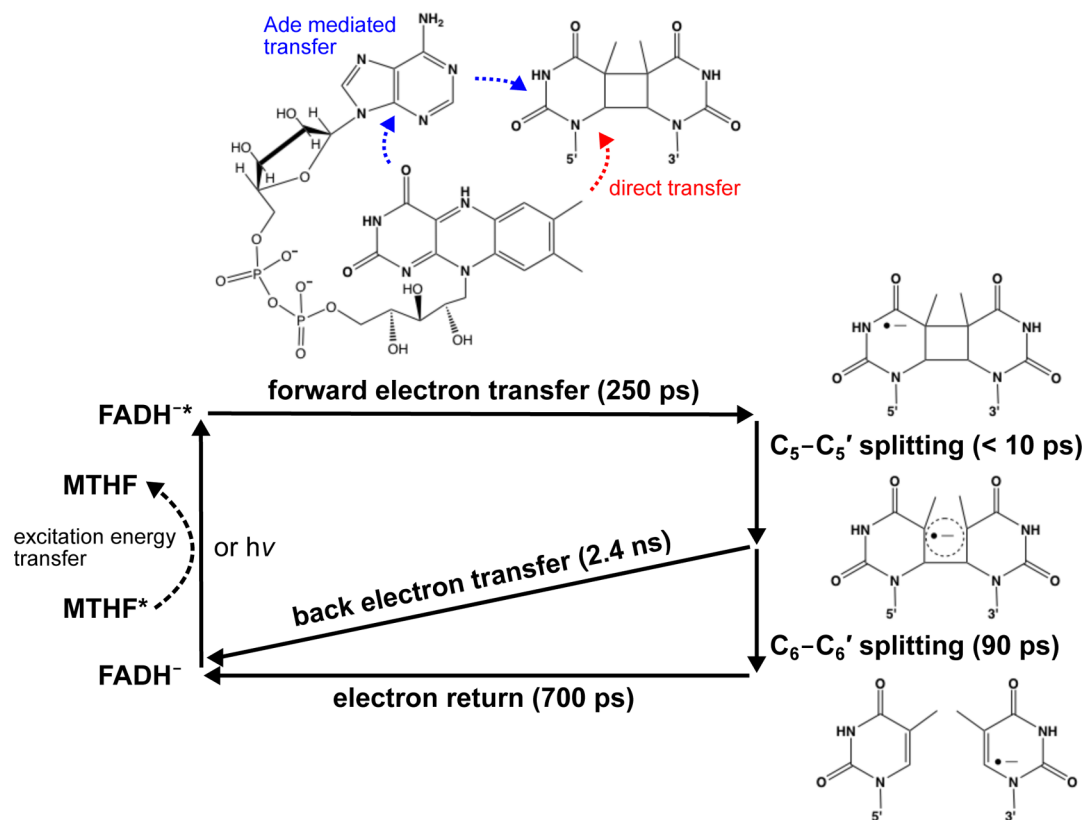
[a]Time constants are taken from ref 6. This photon-powered cyclic electron transfer conserves the number of electrons.[2] Ade and MTHF represent the adenine moiety in the photolyase and a light-harvesting cofactor of methenyltetrahydrofolate, respectively.
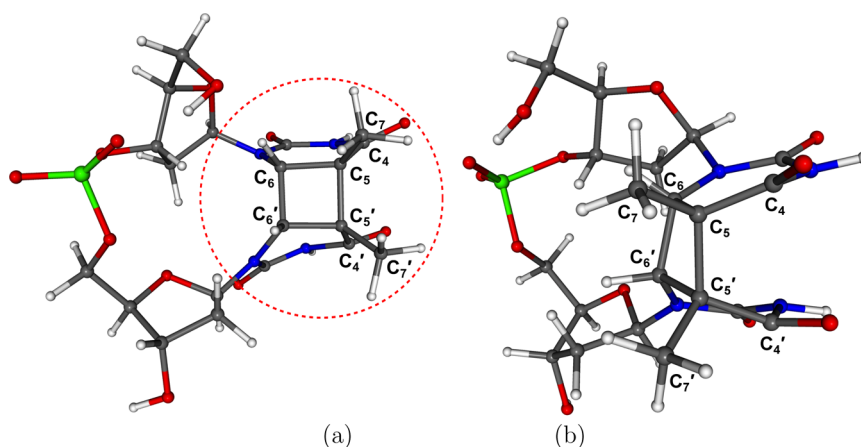
Figure 1. Optimized geometry of TpT$^{\bullet -}$ in the closed form: (a) front and (b) side views. The TT$^{\bullet -}$ moiety is marked by red dashed circle.

excited-state photochemistry and photophysics, and their real-time observation can show transient reaction intermediates[19−21] and reveal reaction mechanisms.[22,23] In a UV/visible pump − Raman probe experiment, a pump pulse excites the molecular system into a valence excited state, and a delayed Raman sequence probes the subsequent rearrangement process. In femtosecond stimulated Raman spectroscopy (FSRS),[24] a Raman probe sequence consists of an off-resonant picosecond probe k_2 and a superimposed femtosecond laser pulse k_3, which stimulates the Raman signal, and successive spectra can be recorded with $\Delta T \approx 20$ fs time intervals with high spectral resolution. Following the original work of Yoshizawa and

Kurosawa,[24] this technique provides a sensitive local probe for ultrafast light-induced processes.[21,25] Different configurations of the FSRS techniques including temporally and spectrally overlapping pulses and resonant Raman processes,[26] and cascading effects in FSRS[27] have been calculated.[28]

Recently we developed an intuitive picture of FSRS signals based on a loop diagram representation.[29,30] The relevant molecular response is expressed by a multipoint correlation function, which can be obtained by microscopic quantum simulations. We have shown that even though the delay time T and spectral resolution are independent experimental knobs, the effective temporal and spectral resolution of the technique

is affected by the probed system dynamics and is inherently limited by the Fourier uncertainty $\Delta\omega\Delta t > 1$;[30] time-resolved vibrational spectra[21,31] are not to be interpreted as instantaneous snapshots of the nuclear frequencies[29] and their interpretation requires a careful analysis.[32,33]

In this paper, we apply this theoretical approach to study how FSRS can monitor the repair dynamics of the cyclobutane thymine dimer radical anion ($TT^{\bullet-}$). The potential energy calculated at the density functional theory (DFT) level involves two minor (<1 kcal/mol) activation barriers for the C_5—C_5' splitting and a main barrier (5.4 kcal/mol) for the C_6—C_6' splitting. Spectroscopic signatures of transient intermediates during the bond rearrangements are identified. The high temporal resolution of the technique allows one to pinpoint the reaction mechanism upon electron uptake by directly monitoring the evolution of characteristic marker bands (i.e., C=O and C=C/C—C stretch vibrations). We find that the simulated FSRS signals for the sequential mechanism show absorptive peaks (~1630 cm^{-1}) of two C_5=C_6 stretch vibrations due to the C_6—C_6' splitting, following the C_5—C_5' splitting. The concerted mechanism, in contrast, yields a dispersive line shape (~1560 cm^{-1}). We further investigate the repair pathway of CPD dinucleotide thymidylyl(3′→5′)-thymidine radical anion ($TpT^{\bullet-}$), which is a first model step toward the CPD lesion embedded in the DNA strand (Figure 1).

2. CPD SPLITTING IN THE THYMINE DIMER RADICAL ANION

In the following, we investigate how FSRS can distinguish between the proposed sequential and concerted splitting mechanisms. We first study $TT^{\bullet-}$ which is a simple model for $TpT^{\bullet-}$ (see the circled moiety of the $TpT^{\bullet-}$ in Figure 1a). Here we focus on the intradimer splitting mechanism subsequent to the forward electron transfer (Scheme 1) as to be discussed in section 2.4, and ignore the CPD-PL enzyme. A potential energy curve of the intradimer splitting is constructed, and the evolution of characteristic vibrational marker bands is identified for the simulation of FSRS signals.

2.1. Optimized Geometries and the Intrinsic Reaction Coordinate (IRC) Path for the Intradimer Splitting Process. The $TT^{\bullet-}$ model has two intradimer bonds: the C_5—C_5' and C_6—C_6' bonds shown in Figure 1a. Geometry optimization yielded three local minima, namely the closed (dimerized) form, the open form,[34] and one intermediate state (INT). The two transition states (TSs) between the local minima were then obtained with the Berny algorithm. The reaction pathways from the TSs to local minima were explored with the intrinsic reaction coordinate (IRC) method,[35] which gives the steepest descent pathway in mass-weighted Cartesian coordinates and yielded another INT and TS. Altogether there are two INTs and three TSs along the complete path toward the splitting (Figure 2). To study the CPD splitting mechanism of the closed form, we constructed a one-dimensional reaction coordinate via the TSs and INTs by connecting the resulting IRCs.[36] Stability of the electronic state along the reaction coordinate was confirmed by the self-consistent-field stability analysis.[37,38] Frequency analysis showed that TSs have a single imaginary frequency mode whereas the other geometries have only real-valued frequencies. All quantum chemical calculations employed the 6-31G* basis set[39,40] and the unrestricted DFT(M05-2X) method[41] to consider the open-shell doublet state of $TT^{\bullet-}$. The M05-2X is a hybrid meta exchange-
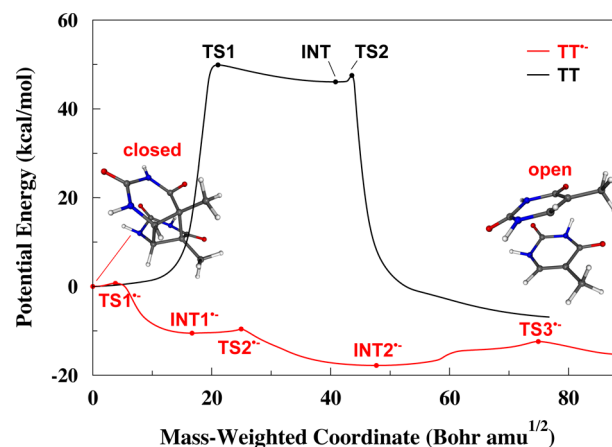
Figure 2. IRC potential energy curves of TT (black) and $TT^{\bullet-}$ (red). Filled circles represent the optimized geometries and the right end structure is the open form. The characteristics of the optimized geometries are specified by closed form (T=T)$^{\bullet-}$, TS1$^{\bullet-}$ [(T=T)$^{\bullet-}$]‡, INT1$^{\bullet-}$ (T⋯T)$^{\bullet-}$, TS2$^{\bullet-}$ [(T⋯T)$^{\bullet-}$]‡, INT2$^{\bullet-}$ (T—T)$^{\bullet-}$, TS3$^{\bullet-}$ [(T⋯T)$^{\bullet-}$]‡, and open form (T$^{\bullet-}$ T), respectively, where the upper and lower lines between two T represent the intradimer C_5—C_5' and C_6—C_6' bonds. A small bump in the energy curve of $TT^{\bullet-}$ around 60 Bohr amu$^{1/2}$ indicates major geometry change along the IRC path; the C_6—C_6' bond splitting starts at this point, as shown in Figure 3a. The energies and the coordinates for the closed forms are set to be zero.

correlation functional, and adequate to study barrier heights of open-shell reactions[41−43] and noncovalent interactions of the nucleic acid base pairs in the JSCH-2005 database[44,45] and of thymine dimers.[46] To test the accuracy of the M05-2X functional for open-shell reaction barriers, we used the highly accurate coupled cluster theory with single and double excitations (CCSD) and the CCSD with perturbative triple excitations (CCSD(T)). The M05-2X barriers agree well with those calculated at both levels of theory (within 1.5 kcal/mol, see Tables 1 and S1), and in particular with those of the

Table 1. Potential Energy Barriers (kcal/mol), Compared to the Preceding Stationary Geometries, in the TT, $TT^{\bullet-}$, and $TpT^{\bullet-}$

	TT	$TT^{\bullet-a}$	$TpT^{\bullet-\,b}$
TS1	49.9	0.7 (2.2, 1.8)	0.2
TS2	1.5	0.9 (−0.4, 0.9)	0.5
TS3	5.4	5.4 (4.9, 5.2)	4.4

^{a}In parentheses are the energies obtained with the CCSD and the CCSD(T) method at the DFT(M05-2X) optimized geometries. ^{b}In a DFT study of an analogue of the $TpT^{\bullet-}$, the barrier (with zero-point energy corrections) for the C_5—C_5' splitting is 1.8 kcal/mol and that for the C_6—C_6' splitting is 3.2 kcal/mol.[11] In QM/MM dynamics studies of CPD embedded in the active site of CPD-PL[14] and in DNA duplex,[18] the C_5—C_5' splitting is barrierless and the free energy barrier of the C_6—C_6' splitting is less than 2.5 kcal/mol.

CCSD(T) theory. These results validate the use of the DFT(M05-2X) method throughout our study. The DFT calculations were carried out with Gaussian 09[47] and molecular visualization with Molekel 5.4.[48] We also studied a synchronous path, where both intradimer bonds split simultaneously. Details and results (Figures S1 − S5) are presented in Supporting Information.

The potential energy along the IRC path of CPD splitting is depicted in Figure 2. As shown in Table 1, the potential energy barriers of TS1$^{\bullet-}$ and TS2$^{\bullet-}$ are less than 1 kcal/mol, while the last TS3$^{\bullet-}$ barrier is the highest (5.4 kcal/mol). In Figure 3a,


(a)

(b)
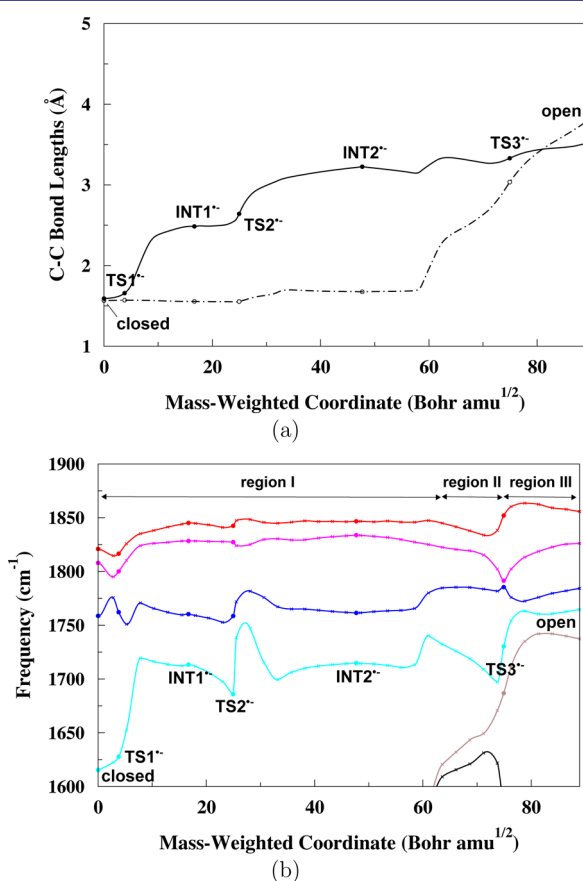
Figure 3. Molecular properties of the TT$^{\bullet-}$ along the IRC path: (a) the C_5—C_5' and the C_6—C_6' bond lengths (solid and broken lines) and (b) frequencies of the 67th–72nd normal modes, which include C≡C/C—C and C≡O stretch vibrations. Filled circles represent the optimized geometries.

the intradimer C_5—C_5' and C_6—C_6' bond lengths are plotted along the IRC path. At INT1$^{\bullet-}$, the C_5—C_5' bond is partially cleaved (2.48 Å) and the C_6—C_6' bond is intact (1.56 Å). As the geometry is relaxed to INT2$^{\bullet-}$, the C_5—C_5' bond fully splits (3.22 Å) but the C_6—C_6' bond remains intact (1.67 Å). In addition, the C_5—C_6—C_6'—C_5' dihedral angle opens by 35.2° and the displacement sum over all atoms in two thymine bases, compared to the free thymine structure, is decreased by 2.44 Å.[36] These indicate that the small TS1$^{\bullet-}$ and TS2$^{\bullet-}$ barriers correspond to the C_5—C_5' splitting and the TS2$^{\bullet-}$ additionally involves an internal rotation around the C_6—C_6' bond and relaxation of thymine structures themselves. Previous quantum chemical calculations had found only one (1.8 kcal/mol) or no TS for the C_5—C_5' splitting,[11,49] probably due to the tiny barriers and the flat potential energy curve. At TS3$^{\bullet-}$, both intradimer bond lengths are larger than 3.0 Å and the main barrier of 5.4 kcal/mol is attributed to the C_6—C_6' splitting. This barrier height is in reasonable agreement with a previous study on the level of B3LYP/6-311++G(2df,p) theory (2.3 kcal/mol).[49] The geometric characteristics are labeled using compact notation in the caption of Figure 2 (e.g., (T⋯T)$^{\bullet-}$ for INT1$^{\bullet-}$ and (T—T)$^{\bullet-}$ for INT2$^{\bullet-}$).

Figure 2 additionally depicts the IRC potential energy of neutral thymine dimer (TT) splitting. It shows a highly activated stepwise mechanism,[50] where TS1 and TS2 are attributed to the C_5—C_5' and the C_6—C_6' splitting. Key geometric parameters of INT are similar to those of INT2$^{\bullet-}$, (T—T)$^{\bullet-}$, as shown in Figure S6 in Supporting Information. The 49.9 kcal/mol TS1 barrier may not be overcome by thermal activation, demonstrating the catalytic function of electron uptake in the radical anionic splitting pathway of TT$^{\bullet-}$; here only small barriers appear and the C_5—C_5' splitting proceeds exothermically. This result agrees well with the experimental findings that electron uptake by the thymine dimer is necessary for both the CPD-PL catalyzed photo-reactivation[6,7] and the spontaneous self-repair.[51]

2.2. Vibrational Marker Bands along the IRC Path. We selected six normal modes (modes 67–72) as characteristic marker bands: four C≡O and the C≡C/C—C stretch vibrations of the TT$^{\bullet-}$. This choice is motivated by the fact
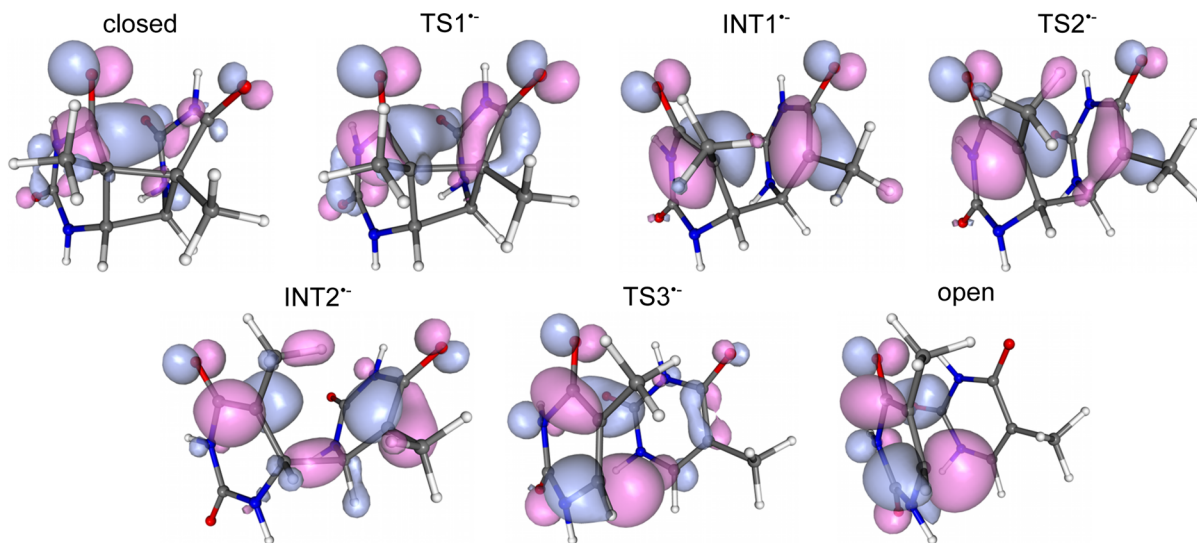
Figure 4. Singly occupied natural orbitals of the TT$^{\bullet-}$. From upper left to lower right, the orbitals at the closed form, TS1$^{\bullet-}$, INT1$^{\bullet-}$, TS2$^{\bullet-}$, INT2$^{\bullet-}$, TS3$^{\bullet-}$, and open form are shown. See Figure S8 for side view.

that these frequencies are sensitive to bond rearrangements along the IRC path as shown in Figure 3b. In addition, the 1600−1900 cm^{-1} C=O and C=C stretch frequencies (see Table S2 for a thymine base) are well separated from those of the other modes, and show relatively strong Raman activity as seen in Figure S7.

In the 1600−1900 cm^{-1} frequency range (Figure 3b), four normal modes appear with a displacement of 0.0 (i.e., the closed form) to about 60 Bohr amu$^{1/2}$, which substantially change along the reaction coordinate, leading to a transient appearance of six modes up to 74.9 Bohr amu$^{1/2}$ (i.e., TS3$^{\bullet-}$) and five modes around the open form. These three regions are hereafter denoted by I, II, and III (see Figure 3b). Considering the geometric characteristics in section 2.1 and Figure 3a, the geometry change in region I corresponds to the C$_5$—C$_5'$ splitting combined with internal rotation around the C$_6$—C$_6'$ bond, while the transition from region I to II initiates the C$_6$—C$_6'$ splitting and that from region II to III finalizes the splitting. The frequency variations in each region can be rationalized by the evolution of relevant molecular orbitals, particularly the singly occupied molecular orbitals (SOMOs); see Figures 4 and S8 for the singly occupied natural orbitals. The closed form has saturated C$_5$—C$_5'$ and C$_6$—C$_6'$ bonds, but no C$_5$=C$_6$ double bonds. This is clear from the doubly occupied bonding orbital built from the lowest unoccupied molecular orbitals (LUMOs) of both thymine bases, which has antibonding π^*(C$_5$—C$_6$) character (see the left orbital diagram in Figure S5). The closed form only has four C=O stretch modes in the 1600−1900 cm^{-1} frequency range. The low 1615 cm^{-1} frequency of one of the C$_4$=O modes, localized in the left thymine in Figure 4, reflects the notable antibonding π^*(C$_4$—O) character of the SOMO; however, as the C$_5$—C$_5'$ bond partially splits, the antibonding character decreases, which strengthens the C$_4$=O bond and leads to a blue shift of the frequency (cyan line in Figure 3b). In the other parts of region I, which mainly correspond to the internal rotation around the C$_6$—C$_6'$ bond, the four C=O stretch modes remain within the 1600−1900 cm^{-1} range and their frequencies do not vary significantly except around TS2$^{\bullet-}$. As the molecular geometry gets closer to INT2$^{\bullet-}$, the SOMO gradually changes from the antibonding interaction between the highest occupied molecular orbitals (HOMOs) of the thymine bases, into the bonding interaction between the LUMOs, as can be seen in Figures 4 and S9. Although the SOMO changes are large, the local electron distribution around the four C=O bonds does not vary significantly and the frequency variations are thus small. Note that only when the geometry passes TS2$^{\bullet-}$, does the SOMO become localized predominantly on one C$_4$=O bond and the C$_6$—C$_6'$ bond (see the sixth panel in Figure S9), resulting in a blue frequency shift of the other C$_4$=O stretch. The Duschinsky rotation matrices[52] were calculated to investigate the mixing of normal modes accompanied by geometry change along the reaction coordinate. Before and after the boundary of regions I and II (see Figure S10), elements of the Duschinsky rotation submatrix of the lower two frequency modes are small, as seen in the lower left panel in Figure S11. In region II, the two normal modes thus completely change into C$_5$=C$_6$ stretch due to the C$_6$—C$_6'$ splitting, and we find a total of six modes in the 1600−1900 cm^{-1} regime. The ~1630 cm^{-1} C$_5$=C$_6$ stretching frequencies are lower than common C=C values (e.g., 1774 cm^{-1} in Table S2). This is because up to TS3$^{\bullet-}$, or [(T···T)$^{\bullet-}$]‡, the SOMO is built from both LUMOs of thymine bases and has strong antibonding π^*(C$_5$—C$_6$) character

(Figure 4). Before and after the boundary of regions II and III (Figure S10), the Duschinsky submatrix of the six modes has large off-diagonal elements (see the lower middle panel in Figure S11). As the geometry passes TS3$^{\bullet-}$ and the C$_6$—C$_6'$ splitting is completed, one C$_5$=C$_6$ stretch vibration, localized in the left thymine in Figure 4, disappears and we only find five modes in the range 1600−1900 cm^{-1}. This is because the SOMO becomes localized in the left thymine; the system can be viewed as consisting of a neutral and a radical anion thymine base, which has five normal modes in the range 1600−1900 cm^{-1} as given in Table S2.

2.3. Two Model Trajectories for the Concerted and the Sequential Mechanism.

We considered an exponential model for the time-dependent IRC:

$$R(\tau) = \begin{cases} R^{\text{open}} + e^{-\tau/\tau_0}(R^{\text{closed}} - R^{\text{open}}) & \tau \geq 0 \\ R^{\text{closed}} & \tau < 0 \end{cases} \quad (1)$$

where R^{closed} and R^{open} are the IRC coordinate values of the closed and open forms and τ_0 is the geometry change time scale. This equation together with the DFT vibrational frequencies $\omega_{ca}(R)$ for a given mode along the IRC path gives a frequency trajectory $\omega_{ca}(\tau)$.

The rate of the C$_5$—C$_5'$ (C$_6$—C$_6'$) splitting depends on how fast the molecular geometry passes through region I (region II). More importantly, the lifetime of INT2$^{\bullet-}$, or (T—T)$^{\bullet-}$, is crucial for distinguishing between the sequential[6] and the concerted nature[14,18] of the intradimer splitting mechanism. In QM/MM simulations,[18] Masson et al. demonstrated that the C$_5$—C$_5'$ bond partially splits within 10−100 fs upon electron uptake. Both intradimer bonds then fully split within 1 ps. After the C$_5$—C$_5'$ splitting, the distance fluctuates around 2.70 ± 0.14 Å with a widespread range from 2.3 to 3.0 Å, and the C$_5$—C$_6$—C$_6'$—C$_5'$ angle fluctuates around 35° ± 4° with a spread of up to 55°. This indicates that the fluctuating geometries are still far from INT2$^{\bullet-}$, whose C$_5$—C$_5'$ distance and C$_5$—C$_6$—C$_6'$—C$_5'$ angle are 3.22 Å and 67.5°, respectively. The second splitting process starts before the completion of the internal C$_6$—C$_6'$ rotation.

We use two trajectories: (A) at τ_0 = 500 fs and (B) at τ_0 = 100 ps. Trajectory A represents the concerted mechanism mentioned above,[14,18] which very rapidly passes INT2$^{\bullet-}$. The frequency changes during the internal C$_6$—C$_6'$ rotation are small. Based on the pioneering work of Langenbacher et al.,[17] Liu et al. suggested an alternative sequential mechanism whereby the C$_5$—C$_5'$ splitting occurs within 10 ps and the C$_6$—C$_6'$ splitting occurs on a time-scale of 90 ps.[6] This slow dynamics implies that the molecular geometry fluctuates around INT2$^{\bullet-}$ before the C$_6$—C$_6'$ splitting. Trajectory B approximately mimics this mechanism.

2.4. FSRS Signals for the Two Model Trajectories.

The FSRS experiment starts with an impulsive actinic pump pulse ε_1 at time 0, which triggers the dynamics. The ultrafast Raman probe ε_3 comes at time T in the presence of the long-duration pump ε_2, and the signal is given by the change in the transmitted intensity of the probe pulse:

$$S_{\text{FSRS}}(\omega, T) = \mathcal{I}P^{(5)}(\omega, T)\varepsilon_3^*(\omega) \quad (2)$$

The fifth-order induced polarization, whose Fourier transform appears in eq 2, is given by a correlation function expression (eq 1 of ref 29). We take $\varepsilon_2(t) = \varepsilon_2 \, e^{-i\omega_2(t-T)}$ to be monochromatic,[53] but the Raman probe has a Gaussian

envelope with center frequency ω_3 and duration σ, $\varepsilon_3(t) = \varepsilon_3\, e^{-(t-T)^2/2\sigma^2 - i\omega_3(t-T)}$. The polarization is then given by

$$P^{(5)}(t,T) = \left(\frac{i}{\hbar}\right)^5 \sum_{a,b,c} |\varepsilon_2|^2 \varepsilon_3 \frac{|V_{ab}|^2 |V_{bc}|^2}{(\omega_2 - \omega_{ba})^2}$$

$$\times \exp[(-i\omega_2 - \gamma_{ca})t] \int_{-\infty}^{t} d\tau_3$$

$$\exp\left[-\frac{(\tau_3 - T)^2}{2\sigma^2} + i\omega_3 T + i(\omega_2 - \omega_3)\tau_3 \right.$$

$$\left. + i\int_{\tau_3}^{t} \omega_{ca}(\tau)d\tau + \gamma_{ca}\tau_3 \right] \tag{3}$$

where ω_{ca} is a vibrational transition frequency in the electronic state prepared by the actinic pulse triggering electron transfer, whereas b is a higher-lying excited state involved in the Raman process (Scheme 2). V_{ij} and ω_{ij} are the transition dipole and

Scheme 2. Level Scheme for the Time-Resolved Raman Process[a]
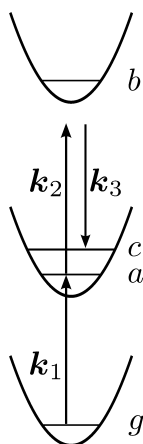
[a] g is the ground state, a and c are vibrational states in the excited electronic state prepared by the actinic pulse, and b is a higher-lying excited state involved in the Raman process.

frequency for the $i \leftarrow j$ transition. The vibrational dephasing time γ_{ca}^{-1} is 532 fs (line width, 10.0 cm^{-1}). The models for the time-dependent frequency $\omega_{ca}(\tau)$ of a specific marker band are discussed in section 2.3. Other parameters are listed in Table 2.

Table 2. Parameters Employed in the FSRS Calculations

ω_3 (cm^{-1})	σ (fs)	τ_0 (fs)	γ_{ca}^{-1} (fs)
$\omega_2 - 1800.0$	20.0	500.0	532.291
		100000.0	

To evaluate $P^{(5)}(t, T)$, we assumed equal Raman activities for the six normal modes (i.e., set the $|\varepsilon_2|^2\varepsilon_3(|V_{ab}|^2|V_{bc}|^2)/(\omega_2 - \omega_{ba})^2$ prefactor in eq 3 to 1) and impulsive electron transfer from photoexcited FADH$^-$ to the neutral thymine dimer. In this way, we separate the pure molecular response from the superimposed initiation process in order to compute the subsequent vibrational dynamics and the microscopic splitting mechanism of the TT$^{\bullet-}$. The detailed electron transfer dynamics and its effect on the dimer signals are beyond the scope of this study. Earlier studies[54] established that the CPD-

PL enzyme primarily stabilizes the FADH$^-$ excited state and slows down the futile back electron transfer.

The simulated FSRS signals for trajectory A are shown in Figure 5a. The peak positions do not resemble the
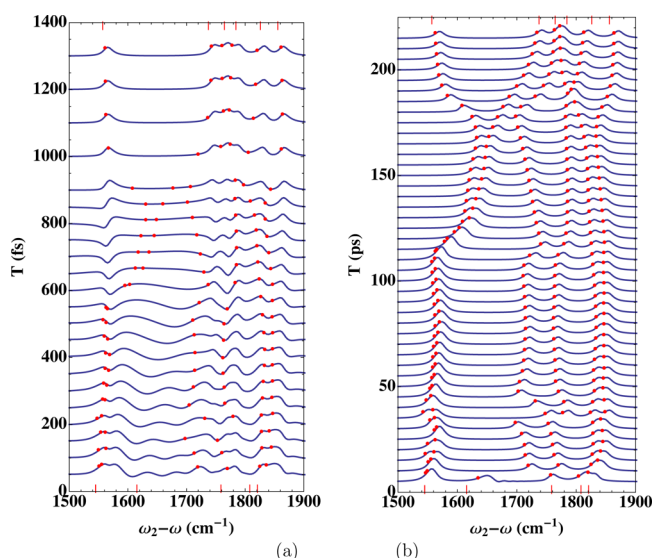
Figure 5. (a) Variation of simulated FSRS signals of TT$^{\bullet-}$ with different delay times T for trajectory A ($\tau_0 = 500$ fs). Time intervals are 50 fs up to 900 fs, and 100 fs later. (b) Variation of simulated FSRS signals for trajectory B ($\tau_0 = 100$ ps). Time interval is 5 ps. Red dots mark instantaneous frequencies. The stick spectra on the horizontal bottom (top) axis represent the initial (final) frequencies.

instantaneous frequencies, and even the number of the peaks is higher than expected from a snapshot picture, in particular at early delay times. This reflects an interference of dispersive and absorptive line shapes,[55] induced by the fast time scale τ_0 of frequency changes ($<\gamma_{ca}^{-1}$). The time-dependent vibrational frequencies cause broadening of the peaks. Dispersive features give a clear characteristic signature of the ultrafast concerted mechanism. No clear signature of the C$_5$—C$_5'$ splitting appears during the geometry change in region I (up to ~500 fs). When the geometry reaches region II, a dispersive line shape is found around 1560 cm^{-1}, which indicates the end of the spontaneous C$_5$—C$_5'$ splitting. It originates from the fast frequency shift (brown line in Figure 3b) due to the end of both intradimer bond splittings and formation of one C$_5$=C$_6$ bond. As the geometry passes region III (>1000 fs), one can see the instantaneous frequencies with high spectral resolution.

The FSRS signals for trajectory B shown in Figure 5b closely resemble the instantaneous frequencies. This is because τ_0 is sufficiently slow, compared to the vibrational dephasing time γ_{ca}^{-1}. The FSRS signal thus directly monitors the bond rearrangement of the sequential mechanism, discussed in section 2.2, at all delay times. In Figure 5b, the C$_5$—C$_5'$ splitting (as well as the internal C$_6$—C$_6'$ rotation) occurs at about 100 ps and the C$_6$—C$_6'$ splitting is reached within another 100 ps. In addition, the partial C$_5$—C$_5'$ splitting is completed within 10 ps, which can be observed as the blue shift of the low-frequency 1615 cm^{-1} C$_4$=O mode. The FSRS signals are sensitive to the forward electron transfer since four C=O stretch frequencies are significantly red-shifted after the electron uptake (see Table S2 and Figure S12).

The snapshot limit has been observed in various systems by different spectroscopic techniques, for example, retinal isomer-

ization studied with FSRS (at sufficiently long delay times $T > 1$ ps),[22,29] dynamics of green fluorescent protein with two-photon fluorescence spectroscopy,[56] dynamics in proteins and enzymes with two-dimensional infrared (2DIR) spectroscopy,[57] photoswitching of a peptide[58] and biomimetric molecule[59] with IR transient absorption spectroscopy. The various techniques provide different controls over the resolution, which results in different signals. The snapshot limit may be achieved with one technique but not with another. Furthermore, some of these techniques can explore larger space of evolving degrees of freedom. In particular, if two degrees of freedom (two nuclear coordinates) become coupled, fast contributions that go beyond the snapshot limit are expected. In this case, the nonadiabatic vibrational dynamics which is normally obtained in a snapshot limit for an individual coordinate becomes untraceable.[60] In the following, we investigate the CPD repair mechanism and discuss the conditions whereby it can be described by a snapshot limit.

3. CPD SPLITTING IN THE THYMIDYLYL(3′→5′)THYMIDINE RADICAL ANION

We next turn to the entire TpT$^{•-}$ dinucleotide shown in Figure 1. The TpT$^{•-}$, whose net charge is $-2e$ and spin multiplicity is 2, is more realistic than the TT$^{•-}$, and their comparison reveals the backbone effect of the DNA strand.[61,62] Geometry optimization, IRC calculations, and frequency analyses along the IRC path were performed in a similar manner to TT$^{•-}$. We introduce a more realistic kinetic model which takes into account the potential energy profile, and investigate the FSRS signals using the stochastic Liouville equation. We compare the resulting signals to the static averaged FSRS signals of transient intermediates.

3.1. Optimized Geometries and the IRC Path: Comparison of TpT$^{•-}$ and TT$^{•-}$. We obtained the geometries of the closed form, two INTs, three TSs, and the open form, as in the TT$^{•-}$. The calculated barrier heights are in reasonable agreement with previous theoretical studies (Table 1).[11,14,18] The potential energy of the TpT$^{•-}$ along the IRC path is shown in Figure 6. Compared with TT$^{•-}$, the energy difference between INT1$^{•-}$ and INT2$^{•-}$ is smaller due to the internal C_6—C_6' rotation and a backbone distortion in INT2$^{•-}$. In addition, the open form is stabilized so that both intradimer splitting processes are exothermic, which agrees with the experimental findings.[6,7,51] The geometric changes along the IRC path and the frequency changes of marker bands of the cyclobutane fragment, shown in Figure S13, are similar to those of the TT$^{•-}$. For example, the geometric change in region I corresponds to the C_5—C_5' splitting and the internal C_6—C_6' rotation, and the change in region II corresponds to the C_6—C_6' splitting. This is because in the TpT$^{•-}$, the SOMO is also localized in the thymine dimer moiety and its change along the IRC path closely resembles TT$^{•-}$, as seen in Figure S14.
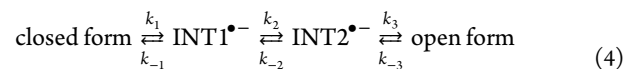
3.2. Sequential First-Order Kinetics and the FSRS Signals. The FSRS signals of TpT$^{•-}$ simulated with the trajectories A and B are similar to those of the TT$^{•-}$ (see Figure S15), except that the dispersive line shape which indicates the passage through region II is found at a higher frequency ($\sim$1720 cm^{-1}) in trajectory A. We now introduce a more realistic kinetic model for the FSRS signals, which takes into account the actual potential energy profile.

We considered a sequential model based on multistep first-order kinetics and transition state theory.[63] We assumed a
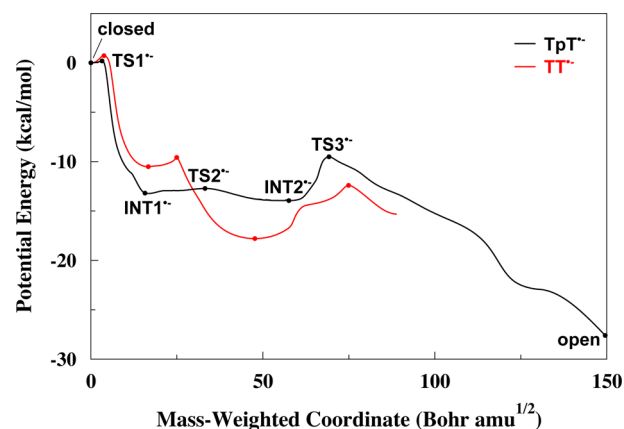
Figure 6. IRC potential energy curve of the TpT$^{•-}$ (black). For reference, the energy curve of the TT$^{•-}$ (red) is shown. Filled dots represent the optimized geometries and the right end structures are the open forms.[34] The characteristics of the optimized geometries are specified by closed form (T=T)$_P^{•-}$, TS1$^{•-}$ [(T=T)$_P^{•-}$]‡, INT1$^{•-}$ (T$\cdots$T)$_P^{•-}$, TS2$^{•-}$ [(T$\cdots$T)$_P^{•-}$]‡, INT2$^{•-}$ (T−T)$_P^{•-}$, TS3$^{•-}$ [(T$\cdots$T)$_P^{•-}$]‡, and open form (T$^{•-}$ T)$_P$, respectively, where the upper and lower lines between two T represent the intradimer C_5—C_5' and C_6—C_6' bonds and the subscript p indicates the phosphate linkage in the TpT$^{•-}$. The energies and the coordinates for the closed forms are set to be zero.

linear sequence of intradimer bond splitting of the TpT$^{•-}$ with back reactions:

$$\text{closed form} \underset{k_{-1}}{\overset{k_1}{\rightleftarrows}} \text{INT1}^{•-} \underset{k_{-2}}{\overset{k_2}{\rightleftarrows}} \text{INT2}^{•-} \underset{k_{-3}}{\overset{k_3}{\rightleftarrows}} \text{open form} \quad (4)$$

These satisfy the rate equation,

$$\frac{\mathrm{d}}{\mathrm{d}t}\rho_{aa}(t) = -K\rho_{aa}(t) \quad (5)$$

where the population $\rho_{aa}(t)$ consists of the concentrations of the four species (e.g., $\rho_{aa}^{(\text{closed})}(t)$) after electron transfer due to the actinic pulse ε_1, and the state a represents the vibrational ground state. The rate matrix K was calculated with the transition state theory at room temperature (see Table S3). The solution of eq 5 is given by

$$\rho_{aa}(t) = U \exp[-K^{\text{diag}}t]U^{-1}\rho_{aa}(0) \quad (6)$$

where U is a transformation matrix, which diagonalizes K into K^{diag}. $\rho_{aa}(0)$ represents the closed form. FSRS signals were calculated using the stochastic Liouville equation.[64,65] This is a convenient approach for computing spectral line shapes of a quantum system coupled to a classical bath. It assumes that the system is affected by the bath, but the bath undergoes an independent stochastic dynamics that is not affected by the system. System/bath entanglement is neglected. The stochastic Liouville equations describe joint dynamics of the system and bath density matrix ρ:

$$\frac{\mathrm{d}\rho}{\mathrm{d}t} = \hat{\mathcal{L}}\rho(t) = -\frac{i}{\hbar}[H, \rho(t)] + \hat{L}\rho(t) \quad (7)$$

Here H is the system Hamiltonian that depends parametrically on the bath and $\hat{L}$ is a Markovian master equation for the bath. We introduce a simple stochastic model, where the bath has four states, namely closed, INT1$^{•-}$, INT2$^{•-}$, and open forms in eq 4.[66] The system has two vibrational states a and c, and the vibrational frequency $\omega_{ca,s}$ is perturbed by the bath state s. The

total density matrix ρ has thus 16 components $|\nu\nu's\rangle\rangle$ which represent the direct product of four Liouville space states $|\nu\nu'\rangle\rangle$, where $\nu,\nu' = a,c$, and four bath states s. The Liouville operator $\hat{\mathcal{L}}$ is diagonal in the vibrational Liouville space and is thus given by four 4×4 diagonal blocks in bath space:

$$[\hat{\mathcal{L}}]_{\nu\nu's,\nu_1\nu_1's'} = \delta_{\nu\nu_1}\delta_{\nu'\nu_1'}([\hat{L}_S]_{s,s'} + \delta_{ss'}[\hat{\mathcal{L}}_S]_{\nu\nu',\nu\nu's}) \quad (8)$$

where $\hat{L}_S = -K$ describes the kinetics given by eq 5 and the coherent part $\hat{\mathcal{L}}_S = -(i/\hbar)\,[H_S,...]$ describes the vibrational dynamics (see eq S1 of Supporting Information). Following the approach outlined in ref 65, we obtain eq S4 for the Stokes contribution to the FSRS signal.

The calculated rate for the C_6—C_6' splitting is slow (14.1 ps), compared to the rates of the two preceding processes (95.4 fs and 1.39 ps), and the kinetics is also closely related with the sequential mechanism proposed from experiments.[6] This is clear from the time-dependent populations of the closed, INT1$^{\bullet-}$, INT2$^{\bullet-}$, and open forms, shown in Figure 7a. The

(a)

(b)
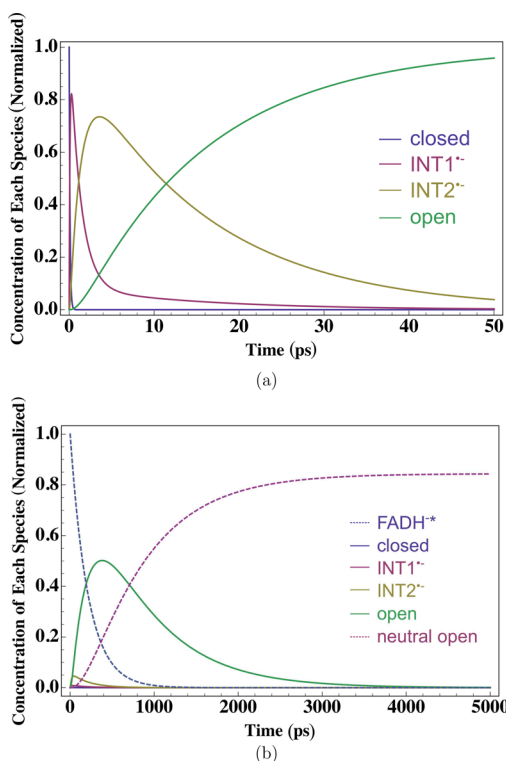
Figure 7. Kinetic evolution of the closed, INT1$^{\bullet-}$, INT2$^{\bullet-}$, and open form (solid blue, purple, yellow, and green) populations of (a) the TpT$^{\bullet-}$ and (b) whole photoreactivation system. In intradimer bond splittings of the TpT$^{\bullet-}$, the initially populated state is the closed form. In entire photoreactivation, the initially populated state is FADH$^-$*, and the concentrations of FADH$^-$* and neutral open form are also shown (broken blue and purple). See Supporting Information for the detailed calculation method.

population of INT2$^{\bullet-}$ reaches its maximum around 4 ps, while the others have much smaller values. The calculated splitting rates are on the same order as the experimental ones by Liu et al.,[6] and at least 10 times faster than the corresponding back reaction rates (Table S3).

The resulting FSRS signals are shown in Figure 8a (see Figure S16a for longer delay times T). Dispersive line shapes are found at $T = 2$ fs, which reflect the blue shift of the 1584

cm^{-1} C_4=O mode, localized in the lower thymine in Figure S14, due to the ultrafast partial C_5—C_5' splitting. After $T = 100$ fs, dispersive line shapes are not seen and the observed peaks follow the frequencies of transient geometries with good resolution. This is because of the slow sequential nature of the kinetics. The signals can thus closely monitor the bond rearrangement. Within 4 ps, four peaks emerge in 1730−1900 cm^{-1}, which indicates that the INT2$^{\bullet-}$ is predominant and the C_5—C_5' splitting is completed. Within 20 ps (Figure S16a), five peaks emerge in 1700−1900 cm^{-1}, which indicates that the subsequent C_6—C_6' splitting is achieved and the open form is predominant. The stochastic Liouville equation is a powerful tool to study the FSRS signals of general kinetic models. The FSRS signal given by eq S4 can be recast as

$$S_{\text{FSRS}}(\omega, T) = \mathcal{I}\frac{-2i}{\hbar^2}\varepsilon_3^*(\omega)|\varepsilon_2|^2 \sum_{a,c}\alpha_{ac}^2$$

$$\sum_s \mathcal{G}_{ac,ac,s}(\omega - \omega_2) \int_{-\infty}^{\infty}\frac{d\Delta}{2\pi}\varepsilon_3(\omega + \Delta)\,e^{i\Delta T}\rho_{aa,s}(-\Delta) \quad (9)$$

where $\rho_{aa}(-\Delta)$ is a Fourier transform of the population of the state a given by eq S9, $\mathcal{G}_{ac,ac}(\omega)$ is a frequency-domain Green's function given by eq S3, and $\sum_s$ represents the sum over species. It follows from eq 9 that the integral over Δ represents a path integral over the bandwidth corresponding to the inverse dephasing time scale (see ref 30). This integral is generally a complex quantity. Therefore, the signal given by eq 9 is governed by both real and imaginary parts of the coherence Green's function $\mathcal{G}_{ac,ac}(\omega)$ and thus contains dispersive features in the spectra. In the limit of slow fluctuations, one can neglect the jump dynamics during the dephasing time. In this case, replacing $\varepsilon_3(\omega + \Delta) \simeq \varepsilon_3(\omega)$, the integral over Δ yields simply $\rho_{aa}(T)$, and we obtain the static averaged signal,

$$S_{\text{FSRS}}(\omega, T) = \sum_a \sum_s S_{\text{FSRS},a}^{(s)}(\omega)\rho_{aa}^{(s)}(T) \quad (10)$$

where

$$S_{\text{FSRS},a}^{(s)}(\omega) = -\mathcal{R}\frac{2}{\hbar^2}|\varepsilon_3(\omega)|^2|\varepsilon_2|^2\sum_c\alpha_{ac}^2\mathcal{G}_{ac,ac,s}(\omega - \omega_2) \quad (11)$$

corresponds to a linear transmission of the Raman pulse. To compute the signal given by eq 10, we first calculate individual signals of the four species, $S_{\text{FSRS},a}^{(s)}(\omega)$. We then average out over the signals with their transient concentrations $\rho_{aa}^{(s)}$, obtained in eq 6. The static averaged FSRS signal (eq 10) contains purely absorptive features due to the neglect of bath stochastic dynamics during the dephasing time. Furthermore, the time evolution is governed in this case by a snapshot of the populations of the excited states. The two signals given by eqs 9 and 10 are thus expected to differ at short time and be similar at longer time. Indeed after $T = 100$ fs, the stochastic Liouville equation and the static average signals (Figures 8 and S16) are virtually identical.

It is interesting how the snapshot limit is connected with nonadiabatic dynamics especially in the context of the CPD repair mechanism. Despite the fact that the mechanism of intradimer C—C bond splitting consists of several adiabatic structural changes, the peak vibrational frequency does follow instantaneously the reaction dynamics. Recently it has been shown that vibrational adiabaticity does not correspond to the
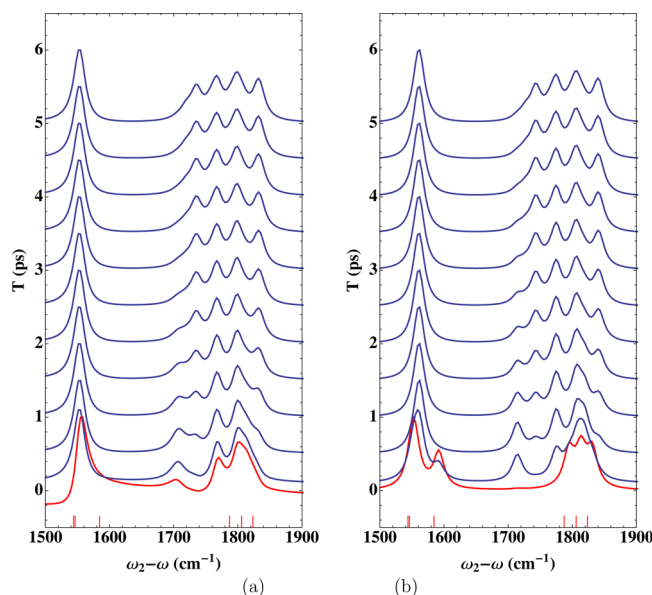
Figure 8. Variation of simulated FSRS signals of the TpT$^{\bullet-}$ with different delay times T. (a) The stochastic Liouville equation (eq 9) and (b) static average (eq 10). The signals at $T = 2$ fs are highlighted in red. After $T = 100$ fs, time interval is 500 fs from $T = 500$ fs up to 5 ps. The stick spectra on the horizontal bottom axis represent the initial frequencies.

snapshot limit.[55] We confirmed this by noting that the dephasing time may be long enough to contain several structural changes, although these changes evolve slowly compared to the vibrational period.

To obtain the total repair quantum yield, we extended the kinetic analysis to consider the entire photoreactivation in the enzyme–substrate complex (see Supporting Information for the details). With the aid of experimental rates of the electron transfer steps (Scheme 1),[6] the repair quantum yield was calculated at 0.844, in good agreement with an experimental yield (0.82).[6] The simulated ultrafast splittings by Masson et al.[14,18] also imply a high repair yield. Thiagarajan et al., however, proposed fast back electron transfer (350 ps) and a lower yield of 0.52.[7] The repair yield depends on a balance between the splitting rates and the back electron transfer rate, which along with the splitting mechanism, is currently under debate. In addition, the effect of CPD-PL protein structure on the splitting rates has not been fully understood; a theoretical study[11] and our calculated rates imply that the CPD-PL does not accelerate the splitting rates decisively, while some experiments suggest the enzyme plays a crucial role in changing the activation energy of splitting.[6,7,54] These issues highlight the importance of direct molecular probe of the splitting dynamics with the FSRS technique. As shown in Figure 7b, the transient concentrations of the closed, INT1$^{\bullet-}$, and INT2$^{\bullet-}$ forms are less than 10% primarily because the forward electron transfer ($k_{\mathrm{FET}}^{-1} = 250$ ps) is slower than the splitting processes. This indicates that the FSRS studies of actual photoreactivation systems require highest detection sensitivity, unlike in an isolated thymine dimer.

4. CONCLUSIONS

We investigated the intermediate and transition states for the intradimer bond splitting of the TT$^{\bullet-}$ and TpT$^{\bullet-}$ by using the DFT(M05-2X) method. The C=O and C=C/C—C stretch vibrations are marker bands, and their changes were rationalized by the SOMO evolution of the transient intermediates. The characteristics of the concerted and the sequential mechanism were studied by model trajectories. The difference in lifetime around the INT2$^{\bullet-}$ geometry, (T—T)$^{\bullet-}$, and consequent differences in the FSRS signals are key signatures for distinguishing between the two proposed mechanisms. We thus demonstrated that FSRS can be a useful tool for probing the underlying molecular mechanism of the intradimer bond splitting by focusing on the time evolution of the marker bands. The direct molecular probe of the actual splitting dynamics is required in order to understand the high repair quantum yield of the photoreactivation, the delicate balance between the splitting processes and the back electron transfer,[6,7] and the effect of CPD-PL protein structure on the splitting rates.[11,54]

■ ASSOCIATED CONTENT

ⓢ Supporting Information

Discussion on the synchronous concerted mechanism of the TT$^{\bullet-}$, the changes of several molecular properties along the IRC paths of the TT$^{\bullet-}$ and TpT$^{\bullet-}$ (potential energies, key geometric parameters, Raman activities, vibrational frequencies, Duschinsky rotation matrices, and SOMOs), FSRS signals of the TpT$^{\bullet-}$, the stochastic Liouville equation, and repair quantum yield calculation in sequential photoreactivation kinetics. This material is available free of charge via the Internet at http://pubs.acs.org.

■ AUTHOR INFORMATION

Corresponding Author
smukamel@uci.edu
Notes
The authors declare no competing financial interest.

■ ACKNOWLEDGMENTS

■ REFERENCES

(1) Sancar, A. *Biochemistry* **1994**, *33*, 2−9.
(2) Sancar, A. *Chem. Rev.* **2003**, *103*, 2203−2237.
(3) Weber, S. *BBA-Bioenergetics* **2005**, *1707*, 1−23.
(4) Yang, W. *Protein Sci.* **2011**, *20*, 1781−1789.
(5) Sinha, R. P.; Häder, D.-P. *Photochem. Photobiol. Sci.* **2002**, *1*, 225−236.
(6) Liu, Z.; Tan, C.; Guo, X.; Kao, Y.-T.; Li, J.; Wang, L.; Sancar, A.; Zhong, D. *Proc. Natl. Acad. Sci. U.S.A.* **2011**, *108*, 14831−14836.
(7) Thiagarajan, V.; Byrdin, M.; Eker, A. P. M.; Müller, P.; Brettel, K. *Proc. Natl. Acad. Sci. U.S.A.* **2011**, *108*, 9402−9407.
(8) Sancar, A. *J. Biol. Chem.* **2008**, *283*, 32153−32157.
(9) Brettel, K.; Byrdin, M. *Curr. Opin. Struct. Biol.* **2010**, *20*, 693−701.
(10) Park, H.-W.; Kim, S.-T.; Sancar, A.; Deisenhofer, J. *Science* **1995**, *268*, 1866−1872.
(11) Chatgilialoglu, C.; Guerra, M.; Kaloudis, P.; Houée-Lévin, C.; Marignier, J.-L.; Swaminathan, V. N.; Carell, T. *Chem.—Eur. J.* **2007**, *13*, 8979−8984.

(12) Hassanali, A. A.; Zhong, D.; Singer, S. J. *J. Phys. Chem. B* **2011**, *115*, 3860−3871.

(13) Hassanali, A. A.; Zhong, D.; Singer, S. J. *J. Phys. Chem. B* **2011**, *115*, 3848−3859.

(14) Masson, F.; Laino, T.; Rothlisberger, U.; Hutter, J. *ChemPhysChem* **2009**, *10*, 400−410.

(15) Kao, Y.-T.; Saxena, C.; Wang, L.; Sancar, A.; Zhong, D. *Proc. Natl. Acad. Sci. U.S.A.* **2005**, *102*, 16128−16132.

(16) MacFarlane, A. W., IV; Stanley, R. J. *Biochemistry* **2003**, *42*, 8558−8568.

(17) Langenbacher, T.; Zhao, X.; Bieser, G.; Heelis, P. F.; Sancar, A.; Michel-Beyerle, M. E. *J. Am. Chem. Soc.* **1997**, *119*, 10532−10536.

(18) Masson, F.; Laino, T.; Tavernelli, I.; Rothlisberger, U.; Hutter, J. *J. Am. Chem. Soc.* **2008**, *130*, 3443−3450.

(19) Mohammed, O. F.; Pines, D.; Dreyer, J.; Pines, E.; Nibbering, E. T. J. *Science* **2005**, *310*, 83−86.

(20) Schreier, W. J.; Schrader, T. E.; Koller, F. O.; Gilch, P.; Crespo-Hernández, C. E.; Swaminathan, V. N.; Carell, T.; Zinth, W.; Kohler, B. *Science* **2007**, *315*, 625−629.

(21) Kukura, P.; McCamant, D. W.; Mathies, R. A. *Annu. Rev. Phys. Chem.* **2007**, *58*, 461−488.

(22) Kukura, P.; McCamant, D. W.; Yoon, S.; Wandschneider, D. B.; Mathies, R. A. *Science* **2005**, *310*, 1006−1009.

(23) Takeuchi, S.; Ruhman, S.; Tsuneda, T.; Chiba, M.; Taketsugu, T.; Tahara, T. *Science* **2008**, *322*, 1073−1077.

(24) Yoshizawa, M.; Kurosawa, M. *Phys. Rev. A* **1999**, *61*, 013808.

(25) Fang, C.; Frontiera, R. R.; Tran, R.; Mathies, R. A. *Nature* **2009**, *462*, 200−204.

(26) Sun, Z.; Lu, J.; Zhang, D. H.; Lee, S.-Y. *J. Chem. Phys.* **2008**, *128*, 144114.

(27) Zhao, B.; Sun, Z.; Lee, S.-Y. *J. Chem. Phys.* **2011**, *134*, 024307.

(28) Lee, S.-Y.; Zhang, D.; McCamant, D. W.; Kukura, P.; Mathies, R. A. *J. Chem. Phys.* **2004**, *121*, 3632−3642.

(29) Mukamel, S.; Biggs, J. D. *J. Chem. Phys.* **2011**, *134*, 161101.

(30) Dorfman, K. E.; Fingerhut, B. P.; Mukamel, S. *Phys. Chem. Chem. Phys.* **2013**, *15*, 12348−12359.

(31) Umapathy, S.; Lakshmanna, A.; Mallick, B. *J. Raman Spectrosc.* **2009**, *40*, 235−237.

(32) Fingerhut, B. P.; Dorfman, K. E.; Mukamel, S. *J. Phys. Chem. Lett.* **2013**, *4*, 1933−1942.

(33) Fingerhut, B. P.; Dorfman, K. E.; Mukamel, S. *J. Chem. Theory Comput.* **2014**, *10*, 1172−1188.

(34) In the TT$^{•−}$, unlike in the TpT$^{•−}$, there is no unique open form due to the lack of DNA backbone. The end-point geometry of an IRC calculation is thus regarded as the open form.

(35) Fukui, K. *Acc. Chem. Res.* **1981**, *14*, 363−368.

(36) A displacement between two molecular structures was evaluated by positioning them in the same *xyz* frame so as not to generate any linear or angular momentum. This method was, for example, employed to evaluate a distance between an optimized geometry and an end-point geometry of IRC calculation, which is useful to connect several IRCs.

(37) Seeger, R.; Pople, J. A. *J. Chem. Phys.* **1977**, *66*, 3045−3050.

(38) Bauernschmitt, R.; Ahlrichs, R. *J. Chem. Phys.* **1996**, *104*, 9047−9052.

(39) Hehre, W. J.; Ditchfield, R.; Pople, J. A. *J. Chem. Phys.* **1972**, *56*, 2257−2261.

(40) Hariharan, P. C.; Pople, J. A. *Theor. Chim. Acta* **1973**, *28*, 213−222.

(41) Zhao, Y.; Schultz, N. E.; Truhlar, D. G. *J. Chem. Theory Comput.* **2006**, *2*, 364−382.

(42) Zhao, Y.; Truhlar, D. G. *Acc. Chem. Res.* **2008**, *41*, 157−167.

(43) Fingerhut, B. P.; Heil, K.; Kaya, E.; Oesterling, S.; de Vivie-Riedle, R.; Carell, T. *Chem. Sci.* **2012**, *3*, 1794−1797.

(44) Hohenstein, E. G.; Chill, S. T.; Sherrill, C. D. *J. Chem. Theory Comput.* **2008**, *4*, 1996−2000.

(45) Jurečka, P.; Šponer, J.; Černý, J.; Hobza, P. *Phys. Chem. Chem. Phys.* **2006**, *8*, 1985−1993.

(46) Banyasz, A.; Douki, T.; Improta, R.; Gustavsson, T.; Onidas, D.; Vayá, I.; Perron, M.; Markovitsi, D. *J. Am. Chem. Soc.* **2012**, *134*, 14834−14845.

(47) Frisch, M. J.; Trucks, G. W.; Schlegel, H. B.; Scuseria, G. E.; Robb, M. A.; Cheeseman, J. R.; Scalmani, G.; Barone, V.; Mennucci, B.; Petersson, G. A.; Nakatsuji, H.; Caricato, M.; Li, X.; Hratchian, H. P.; Izmaylov, A. F.; Bloino, J.; Zheng, G.; Sonnenberg, J. L.; Hada, M.; Ehara, M.; Toyota, K.; Fukuda, R.; Hasegawa, J.; Ishida, M.; Nakajima, T.; Honda, Y.; Kitao, O.; Nakai, H.; Vreven, T.; Montgomery, J. A., Jr.; Peralta, J. E.; Ogliaro, F.; Bearpark, M.; Heyd, J. J.; Brothers, E.; Kudin, K. N.; Staroverov, V. N.; Kobayashi, R.; Normand, J.; Raghavachari, K.; Rendell, A.; Burant, J. C.; Iyengar, S. S.; Tomasi, J.; Cossi, M.; Rega, N.; Millam, J. M.; Klene, M.; Knox, J. E.; Cross, J. B.; Bakken, V.; Adamo, C.; Jaramillo, J.; Gomperts, R.; Stratmann, R. E.; Yazyev, O.; Austin, A. J.; Cammi, R.; Pomelli, C.; Ochterski, J. W.; Martin, R. L.; Morokuma, K.; Zakrzewski, V. G.; Voth, G. A.; Salvador, P.; Dannenberg, J. J.; Dapprich, S.; Daniels, A. D.; Farkas, O.; Foresman, J. B.; Ortiz, J. V.; Cioslowski, J.; Fox, D. J. *Gaussian 09*, Revision C.01; Gaussian Inc.: Wallingford, CT, 2009.

(48) Varetto, U. *Molekel 5.4*; Swiss National Supercomputing Centre: Lugano, Switzerland, 2009.

(49) Durbeej, B.; Eriksson, L. A. *J. Am. Chem. Soc.* **2000**, *122*, 10126−10132.

(50) Boggio-Pasqua, M.; Groenhof, G.; Schäfer, L. V.; Grubmüller, H.; Robb, M. A. *J. Am. Chem. Soc.* **2007**, *129*, 10996−10997.

(51) Chinnapen, D. J.-F.; Sen, D. *Proc. Natl. Acad. Sci. U.S.A.* **2004**, *101*, 65−69.

(52) Duschinsky, F. *Acta Physicochim. U.R.S.S.* **1937**, *7*, 551−566.

(53) Reference 55 explicitly treats a Raman pump pulse of finite duration.

(54) Kao, Y.-T.; Song, Q.-H.; Saxena, C.; Wang, L.; Zhong, D. *J. Am. Chem. Soc.* **2012**, *134*, 1501−1503.

(55) Cina, J. A.; Kovac, P. A. *J. Phys. Chem. A* **2013**, *117*, 6084−6095.

(56) Langhojer, F.; Dimler, F.; Jung, G.; Brixner, T. *Biophys. J.* **2009**, *96*, 2763−2770.

(57) Thielges, M. C.; Fayer, M. D. *Acc. Chem. Res.* **2012**, *45*, 1866−1874.

(58) Bredenbeck, J.; Helbing, J.; Kumita, J. R.; Woolley, G. A.; Hamm, P. *Proc. Natl. Acad. Sci. U.S.A.* **2005**, *102*, 2379−2384.

(59) Briand, J.; Bräm, O.; Réhault, J.; Léonard, J.; Cannizzo, A.; Chergui, M.; Zanirato, V.; Olivucci, M.; Helbing, J.; Haacke, S. *Phys. Chem. Chem. Phys.* **2010**, *12*, 3178−3187.

(60) Branigan, E. T.; Halberstadt, N.; Apkarian, V. A. *J. Chem. Phys.* **2011**, *134*, 174503.

(61) Schreier, W. J.; Kubon, J.; Regner, N.; Haiser, K.; Schrader, T. E.; Zinth, W.; Clivio, P.; Gilch, P. *J. Am. Chem. Soc.* **2009**, *131*, 5038−5039.

(62) Desnous, C.; Babu, B. R.; Moriou, C.; Mayo, J. U. O.; Favre, A.; Wengel, J.; Clivio, P. *J. Am. Chem. Soc.* **2008**, *130*, 30−31.

(63) Pechukas, P. *Annu. Rev. Phys. Chem.* **1981**, *32*, 159−177.

(64) Šanda, F.; Mukamel, S. *J. Chem. Phys.* **2006**, *125*, 014507.

(65) Dorfman, K. E.; Fingerhut, B. P.; Mukamel, S. *J. Chem. Phys.* **2013**, *139*, 124113.

(66) The potential energy barriers of TS1$^{•−}$ and TS2$^{•−}$ are less than 1 kcal/mol (Table 1), which are comparable to the thermal energy. This indicates that in reality, kinetics would not be determined by Markovian transitions, but rather stochastic dynamics with some degree of long-term non-Markovian memory is to be expected. It is, however, likely that this does not affect the main conclusion discussed below: at early delay times, dispersive line shapes are observed, while at longer delay times, static averaged signals only with absorptive line shapes are obtained, as already revealed by the stochastic Liouville equation (Figure 8a).

14810

dx.doi.org/10.1021/ja5063955 | *J. Am. Chem. Soc.* 2014, 136, 14801−14810